



ELSEVIER

Available online at [www.sciencedirect.com](http://www.sciencedirect.com)

SCIENCE @ DIRECT®

Physica A 323 (2003) 107–123

PHYSICA A

[www.elsevier.com/locate/physa](http://www.elsevier.com/locate/physa)

# Fractal analysis of lyotropic lamellar liquid crystal textures

S.V. Muniandy\*, C.S. Kan, S.C. Lim, S. Radiman

*School of Applied Physics, Faculty of Science & Technology, University of Kebangsaan Malaysia, UKM Bangi, Selangor 43600, Malaysia*

Received 16 September 2002; received in revised form 7 December 2002

---

## Abstract

We apply fractal analysis to study the birefringence textures of lyotropic lamellar liquid crystal system (water/cethylpyridinium chloride/decanol). Birefringence texture morphologies are important as they provide information on the molecular ordering as well as defect structures and therefore has been adopted as a standard method in characterizing different phases of liquid crystals. The system under consideration shows a gradual morphological transition from mosaic to oily streak structures and then to maltese cross texture when the water content is increased. Since these textures are the characteristic fingerprints for the lyotropic lamellar phases, it is necessary to have robust techniques to obtain image quantifiers that can characterize the morphological structure of the textures. For this purpose we employ three different approaches namely the Fourier power spectrum for monofractal analysis, the generalized box-counting method for multifractal analysis and multifractal segmentation technique for estimating the space-varying local Hurst exponents. The relationships between estimated image parameters such as the spectral exponent, the Hurst exponent and the fractal dimension with respect to patterns observed in the birefringence textures are discussed.

© 2003 Elsevier Science B.V. All rights reserved.

PACS: 47.53.+n; 61.30; 64.70.Md

*Keywords:* Fractals; Liquid crystals; Textures; Self-similar processes

---

---

\* Corresponding author.

E-mail address: [msithi@pkriscc.ekm.my](mailto:msithi@pkriscc.ekm.my) (S.V. Muniandy).

## 1. Introduction

Textural analysis has contributed significantly in the characterization of complex disordered materials, especially with the continuing efforts to link the physical properties of interest to those textural parameters that are extracted from the images [1]. Fractal geometry supplies a versatile and powerful theoretical framework to describe complex surfaces [2]. Fractal models have been successfully applied to the quantitative description of microstructures such as surface roughness [3], grain boundaries in disordered metals and alloy, classification of shape and textures [4,5], characterization of thin film surfaces [6,7]. Even though there are increasing number of studies on various fractal growth phenomena in soft condensed materials, only few have discussed on the applications of fractal analysis to the birefringence patterns observed in optical polarized microscopy experiments for phase characterization of liquid crystals systems. Self-assembly of amphiphilic molecules in aqueous solutions usually in the presence of co-surfactants or short chain aliphatic molecules form a vast variety of complex structures [8,9]. In this study, we shall restrict the analysis to lamellar  $L_\alpha$  phase, which is one of the most studied lyotropic liquid crystal phases [10]. These phases are modelled as infinite parallel bilayer membranes consist of one or more amphiphilic molecules periodically stacked in space separated by a solvent. Lamellar phases exhibit long range smectic order and show characteristic birefringent textures when observed under polarizing light microscope. The morphological features of the liquid crystal textures are unique with respect to their phases and are often used for phase recognition purposes. Nevertheless, successful identification of complex mixtures of phases is often difficult and requires vast experiences. It is therefore, desirable to develop robust quantitative techniques for computer aided texture analysis for efficient characterization of the surface morphologies.

Fractal-based techniques for texture analysis offer many advantages especially for surfaces that exhibit self-similar properties. For example, the fractal dimension is directly linked to surface roughness. Furthermore, the underlying scale invariance that is observed in most complex surfaces can often be translated into power-law behaviors in certain image variables. Spectral methods focus on the properties of Fourier spectra hereby capturing global information about the image ‘energy’ distribution across scales or wavenumbers. Power-law spectral behavior implies scale invariance or simply indicates fractal characteristic. If the scaling exponent of the power-law behavior remains a constant over a certain range of scales, then the object is said to be globally self-similar. Self-similarity can be characterized using various geometrically related parameters such as the Hurst exponent  $H$  and spectral exponent  $\alpha$ , which can be linked to fractal dimension using a particular model or stochastic process as the generator of such morphologies. Hurst exponent and the fractal dimension are useful quantifiers for analyzing surface roughness and texture segmentation. However, a single fractal dimension is insufficient for describing a surface that exhibits anisotropy or inhomogeneous scaling properties. Under such circumstances, one has to generalize the concept of monofractal to multifractal to cater for the heterogeneity of the surfaces that may be formed by the coexistence of many fractal sets of different fractal dimensions. Other technique such as the gray-level cocurrence matrix (GLCM) [11] also offers the possibility of characterizing anisotropy.

In this paper, we investigate the scaling behaviors of the image textures of lyotropic lamellar liquid crystal system in gray-level as well as black and white image formats. Optical studies of the birefringence patterns of liquid crystal offer useful information on the defect structures and thus it has been adopted as a standard method in characterizing different phases [12]. Birefringent textures in liquid crystals are due to the spatial variation of the director field which are visualized through the optical contrast between regions with different orientations of this axis with respect to a particular reference plane. The molecules in liquid crystals usually have characteristic anisotropic optical properties. Thus by passing polarized light through a liquid crystal specimen, one can detect the alignment of the molecules. Maximum birefringence is observed when the angle between the specimen principal plane and the analyzer permitted electric vector vibrational direction overlap. Interference between the recombining white light rays in the analyzer vibration plane often produces a spectrum of color, which is due to residual complementary colors arising from destructive interference of white light. In order to perform quantitative studies on the texture images, the original color images are converted into gray-level [0-255] format with the brighter regions corresponding to the constructive interference patterns in the birefringence textures.

We have chosen the lyotropic lamellar liquid crystal quasi-ternary system (water/cetylpyridinium chloride/decanol) that shows a gradual morphological transition from mosaic to oily streak structures and then to maltese cross texture upon increasing the water content. We use the monofractal analysis based on two-dimensional (2D) Fourier spectral technique on gray-level images to investigate the power-law scaling behavior. This is followed by the estimation of the generalized box-counting dimension using the multifractal analysis on black and white images. The black pixels correspond to textures with gray-level pixel values from 77 and above (based on 30% thresholding). An alternative approach to studying multifractality or anisotropic local scaling in the gray-level images based on multifractional Brownian motion (MBM) with space-varying Hurst exponents is also given.

## 2. Experimental method and image preprocessing

The lyotropic liquid crystal under consideration is a quasi-ternary system consisted of cationic surfactant cetylpyridinium chloride (Fluka, 98%), decanol (Fluka, 99.5%) and doubly distilled and deionized water (resistivity 18.2 M $\Omega$ ). The samples are prepared by mixing the weighed components thoroughly in screw-capped glass tubes at room temperature (25°C). The surfactant to decanol ratio is fixed at 1:1 for all the samples such that changes in the lamellar mesophases would only be due to variations in the water content of the mixture, denoted by (wt%). Six samples are prepared by varying the water content at the amount of 2% for each sample, starting with 20 wt%. Attempts to prepare samples with lower water contents resulted in low viscosity, thus jeopardizing the homogeneity of the samples. In order to ensure the homeotropic alignment of the sandwiched lamellar phase, all glassware used in the experiment are cleaned with chromic acid and rinsed with deionized distilled water. Fig. 1 shows the phase diagram of the prepared samples.

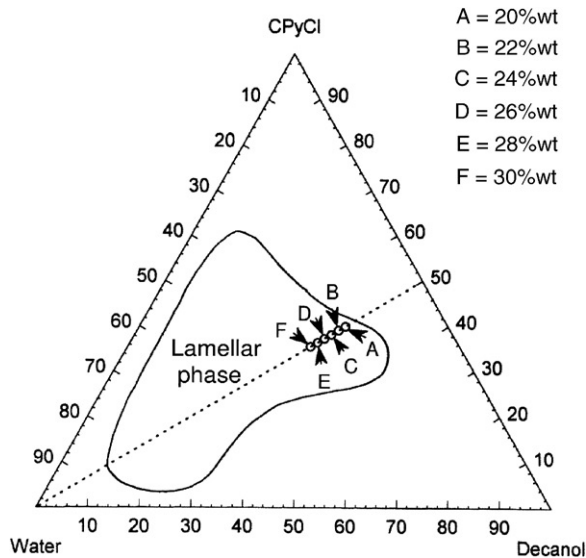


Fig. 1. The phase diagram for lyotropic lamellar liquid crystal quasi-ternary system water/cethylpyridinium chloride/decanol.

Thin layers of samples, each with fixed thickness of  $13\ \mu\text{m}$  is obtained by using mylar spacer carefully placed between glass slides and cover slips to avoid shear induced textures. All the samples are then left to achieve equilibrium such that no further changes in textures are observed before the images are taken. The samples are examined under polarizing microscope (Nikon, Optishot-2). The textures images are captured using a Nikon FX35DX optical camera with exposure controller, which is attached to the microscope.

In order to ensure that the textures of the liquid crystal are indeed lamellar phases, freeze fracture electron microscopy is employed. Replicas of the sample are prepared by rapidly plunging a thin layer ( $\sim 20\ \mu\text{m}$ ) of the sample sandwiched in between two copper foils. Liquid nitrogen is used to freeze the microstructures. The frozen sample are then fractured at  $\sim 100^\circ\text{C}$  in vacuum ( $10^{-7}$  mbar) inside a Balzer O60 freeze etching unit. The replicas are made by sputting platinum–carbon film at an angle of  $90^\circ$  and platinum unidirectional shadowing at an angle of  $45^\circ$ . The replicas are then washed with acetone for several minutes and fished onto a holey grid. The replicas are later dried for 30 min at room temperature and later observed under a transmission electron microscope (Philips, CM120BioTwin).

The original color images are converted to gray-level images and clipped to form a set of square images with uniform size of  $512 \times 512$  pixels. These images are further corrected to mimic uniform illumination. Gray-level images as shown in Fig. 2 will be used for the 2D power spectrum analysis. The black and white images as shown in Fig. 3 are obtained by thresholding the uniformed gray-level images at an appropriate level and this set of images will be used for generalized box-counting multifractal

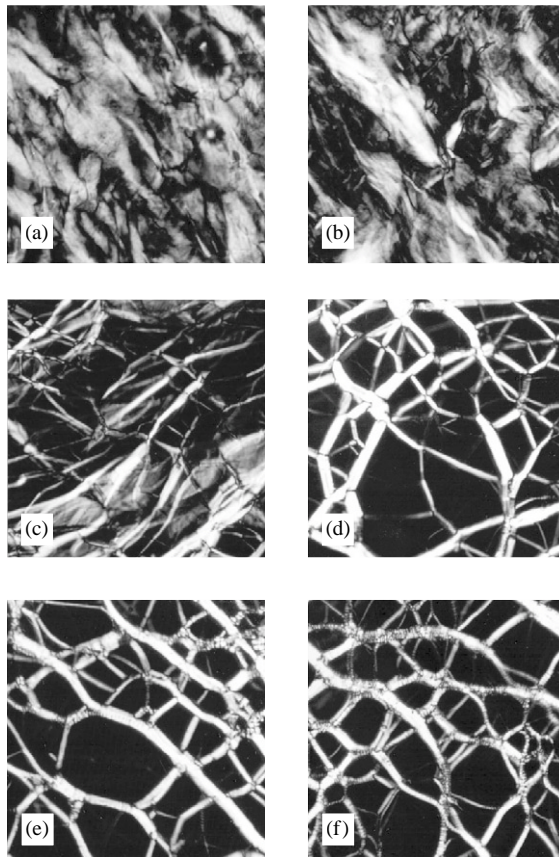


Fig. 2. Gray-level images of the textures for varying water contents: (a) 20% wt; (b) 22% wt; (c) 24% wt; (d) 26% wt; (e) 28% wt; (f) 30% wt.

analysis. We prepare a set of four images obtained by partitioning the original image into four quadrants of  $256 \times 256$  pixels for each of the compositions. Ensemble averages of the scaling parameters and their estimation error bars are obtained.

### 3. Monofractal analysis

#### 3.1. Fractional Brownian sheet

Many natural and man-made surfaces exhibit self-similarity at different scales or resolutions in the form of [2]

$$M(ar) = a^{f(D)}M(r), \quad (1)$$

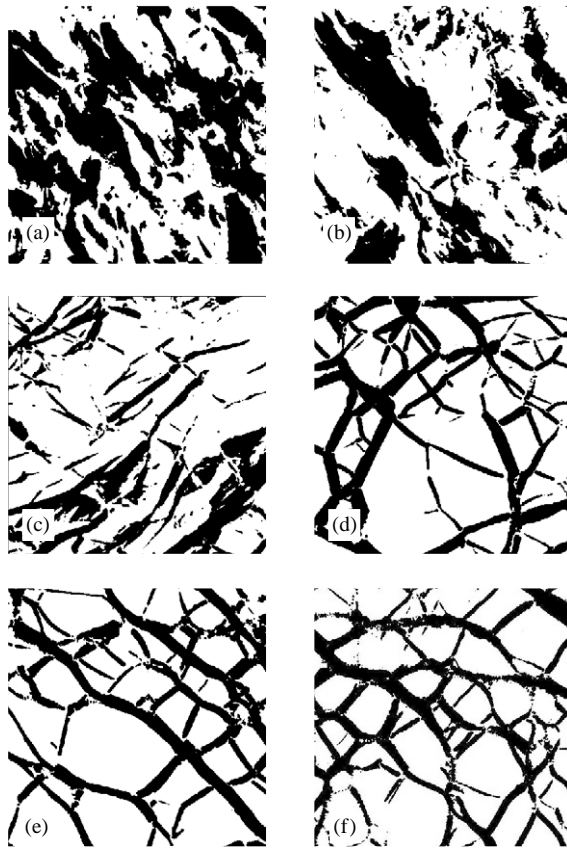


Fig. 3. Black and white images of the textures with varying water contents: (a) 20% wt; (b) 22% wt; (c) 24% wt; (d) 26% wt; (e) 28% wt; (f) 30% wt.

where  $M(r)$  represents any measurable property of the fractal object (for example perimeter, surface area, mass),  $r$  represents the length of the measured metric property,  $a$  is the scaling factor, and  $f(D)$  is a linear function of the fractal dimension.

In modelling natural or man-made textures, various models for generating fractal curves and surfaces have been suggested and examples include iterated function system (IFS), Weierstrass function and a number of self-similar stochastic processes such as fractional Brownian motion (FBM) and fractional Levy motion (FLM) [2]. The FBM [13] is defined as

$$B_H(x) = \frac{1}{\Gamma(H + 1/2)} \left\{ \int_{-\infty}^0 (x - x')^{H-1/2} - (-x')^{H-1/2} dB(x') + \int_0^x (x - x')^{H-1/2} dB(x') \right\}, \quad (2)$$

where the Hurst exponent  $0 < H < 1$ ,  $B(\cdot)$  is Brownian motion and  $H$ -self-similarity refers to the statistical invariant property under scale transformation namely  $\{B_H(ax)\} \equiv \{a^H B_H(x)\}$ . For modelling of surface textures, it is necessary to employ 2D FBM or fractional Brownian surface [14,15]. A direct way to obtain 2D representation of FBM is to use tensor product of two one-dimensional (1D) FBM, namely  $B_H(x, y) = B_H(x) \otimes B_H(y)$ . Nevertheless, a more natural candidate for isotropic random surface generator is given by the fractional Brownian sheet (FBS) denoted by  $B_H(\mathbf{x})$ . FBS is obtained by considering the generalization of the 2D Brownian field  $B(\mathbf{x})$ ,  $\mathbf{x} = (x_1, x_2) \in R^2$ , which is a two-parameter Gaussian random process with zero mean and the following covariance

$$\langle B(\mathbf{x})B(\mathbf{y}) \rangle = \frac{1}{2} [\|\mathbf{x}\| + \|\mathbf{y}\| - \|\mathbf{x} - \mathbf{y}\|] , \tag{3}$$

where  $\|\cdot\|$  denotes euclidean norm  $\|\mathbf{x}\| = (x_1^2 + x_2^2)^{1/2}$ . The covariance of FBS is then written as

$$\langle B_H(\mathbf{x})B_H(\mathbf{y}) \rangle = \frac{1}{2} [\|\mathbf{x}\|^{2H} + \|\mathbf{y}\|^{2H} - \|\mathbf{x} - \mathbf{y}\|^{2H}] . \tag{4}$$

It follows that the variance of the FBS is

$$\langle (B_H(\mathbf{x}))^2 \rangle = \|\mathbf{x}\|^{2H} \tag{5}$$

and that of the increment processes is

$$\langle (B_H(\mathbf{x}) - B_H(\mathbf{y}))^2 \rangle = \|\mathbf{x} - \mathbf{y}\|^{2H} . \tag{6}$$

Note that  $B_H(\mathbf{x})$  is an isotropic Gaussian process with stationary increments. In addition, it generates a self-similar surface that exhibits the following property:

$$B_H(a\mathbf{x}) = a^H B_H(\mathbf{x}) \quad \text{for } a > 0 . \tag{7}$$

The properties of self-similarity and stationary increments allow one to associate with  $B_H(\mathbf{x})$  a generalized spectral density of the form  $\sim |\mathbf{k}|^{-(2H+2)}$  where the surface fractal dimension is given by  $D = 3 - H$ . Strictly speaking, power spectrum can only be associated to stationary random field that is shift invariant. However, there exist various time-frequency or time-scale representations [16], which can be adopted for space-dependent power spectra. One common method for the determination of the power spectrum of a non-stationary random field is to use the Wigner–Ville distribution [17]. Let  $R(\mathbf{x}, \mathbf{y})$  denotes the covariance of FBS and the correlation between two points separated by an interval of size  $z$  is written as

$$R\left(\mathbf{x} - \frac{\mathbf{z}}{2}, \mathbf{x} + \frac{\mathbf{z}}{2}\right) = \frac{1}{2} \left( \left\| \mathbf{x} + \frac{\mathbf{z}}{2} \right\|^{2H} + \left\| \mathbf{x} - \frac{\mathbf{z}}{2} \right\|^{2H} - \|\mathbf{z}\|^{2H} \right) . \tag{8}$$

The Wigner–Ville distribution of  $B_H(\mathbf{x})$  is then defined as

$$W_{B_H}(\mathbf{x}, \mathbf{k}) = \int_{\mathcal{R}^2} e^{-i\mathbf{k}\cdot\mathbf{z}} R\left(\mathbf{x} - \frac{\mathbf{z}}{2}, \mathbf{x} + \frac{\mathbf{z}}{2}\right) d\mathbf{z} . \tag{9}$$

Since the Fourier transform of the distribution  $\|\mathbf{z}\|^{2H} \sim |\mathbf{k}|^{-2H-2}$ , one gets

$$W_{B_H}(\mathbf{x}, \mathbf{k}) = C [1 - 2^{1-2H} \cos(2\mathbf{k} \cdot \mathbf{x})] \frac{1}{|\mathbf{k}|^{2H+2}} , \tag{10}$$

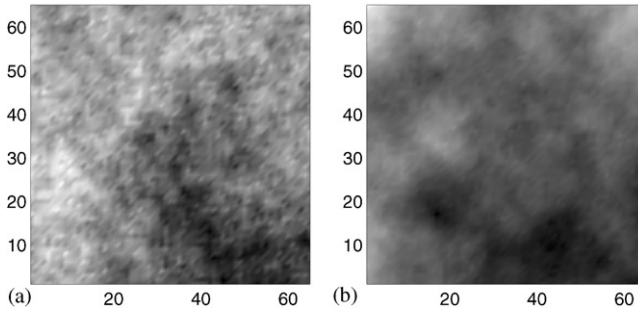


Fig. 4. Surface textures of FBS for: (a)  $H = 0.3$ , and (b)  $H = 0.75$ .

where  $\mathbf{k} \cdot \mathbf{x} = k_1x_1 + k_2x_2$  and  $C$  is a  $H$ -dependent constant. In order to obtain a global power-spectrum from  $W_{BH}(x, k)$ , it is necessary to consider its space average over an area  $[0, X_1] \times [0, X_2]$ :

$$\begin{aligned} \bar{W}_{BH}(\mathbf{x}, \mathbf{k}) &= \frac{1}{X_1X_2} \int_0^{X_1} \int_0^{X_2} C [1 - 2^{1-2H} \cos(2\mathbf{k} \cdot \mathbf{x})] \frac{dx_1 dx_2}{|\mathbf{k}|^{2H+2}} \\ &= \frac{C}{X_1X_2} \left[ X_1X_2 - \frac{2^{1-2H}}{k_1k_2} (\sin(2k_1X_1) \sin(2k_2X_2)) \right. \\ &\quad \left. - \cos(2k_1X_1) \cos(2k_2X_2) + 1 \right] \frac{1}{|\mathbf{k}|^{2H+2}} . \end{aligned} \tag{11}$$

In the large  $X_1, X_2$  limit, the average power spectrum of a surface is given by

$$P(|\mathbf{k}|) = \lim_{X_1, X_2 \rightarrow \infty} \bar{W}_{BH}(\mathbf{x}, \mathbf{k}) = \frac{C}{|\mathbf{k}|^{2H+2}} . \tag{12}$$

Isotropic monofractal random surfaces as shown in Fig. 4 for  $H = 0.3$  and  $0.75$  have been generated using the FBS model.

In the next section, we shall confine our analysis based on FBS model to woolly textures observed for samples with low water concentrations only. The oily streaks may require completely different model that takes the formation of the cross-linked network textures into consideration.

### 3.2. Power spectrum analysis

Fourier spectral analysis has been used extensively in the study of self-similar processes that exhibit power-law power spectrum of the form  $P(f) \sim f^{-\alpha}$  where  $f$  is the frequency and  $\alpha$  is the spectral exponent. For a fractal time series  $X(t)$ , a crude estimate of the exponent is usually obtained from the slope of the log squared modulus of the Fourier transform  $\hat{X}(f)$  versus log frequency  $f$  plot.

The spectral method can be extended to 2D gray-level images with pixel intensity  $I(x, y)$  and it has been widely used for characterizing surface roughness [18,19]. The power spectrum of a gray-level image is obtained by integrating the 2D power spectrum

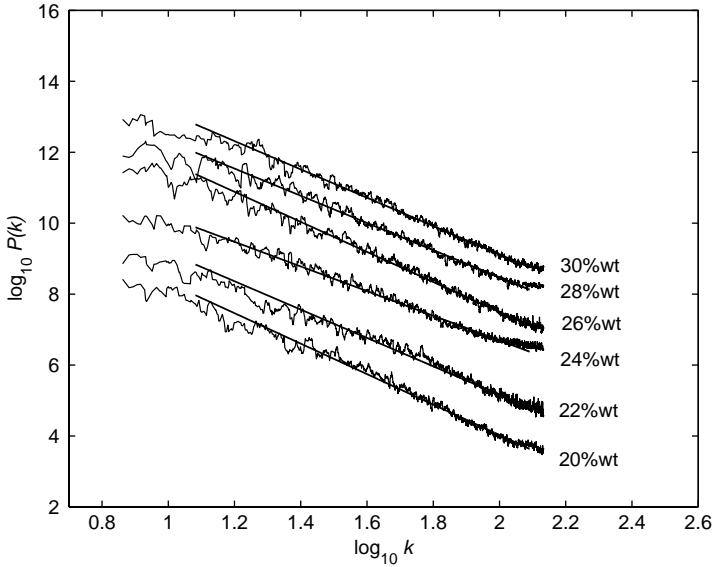


Fig. 5. Power spectrum of gray-level images.

Table 1  
Spectral exponents of the 2D power spectra of gray-level images

Samples (wt%)	Spectral exponents, $\alpha$	Hurst exponent, $H(=\frac{\alpha-d_s}{2})$	Filling factor, $d_s$
20	$3.89 \pm 0.13$	$0.94 \pm 0.03$	2
22	$3.31 \pm 0.12$	$0.66 \pm 0.03$	2
24	$3.35 \pm 0.10$	$0.68 \pm 0.02$	2
26	$3.76 \pm 0.12$	$0.38 \pm 0.01$	3
28	$3.83 \pm 0.09$	$0.46 \pm 0.01$	3
30	$4.01 \pm 0.08$	$0.50 \pm 0.01$	3

$P(k_x, k_y) = |\hat{I}(k_x, k_y)|^2$ , along the circles of constant spatial frequency,  $|k| = \sqrt{k_x^2 + k_y^2}$ . This gives the one-dimensional power spectrum density  $P(|k|)$  plot starting with the zero spatial frequency (also known as the DC component) and increasing to the Nyquist frequency,  $k_{Nq}$ , where  $k_{Nq} = (k_{x,Nq}^2 + k_{y,Nq}^2)^{1/2}$  [20]. The Nyquist frequency is the highest frequency which can be accurately represented and is defined as one-half of the sampling rate or pixel resolution in the case of an image. This image power spectrum corresponds to the average power spectrum of a surface given by (12). Fig. 5 shows the log–log plot of the power spectra of the gray-level images and the slopes of the least-square regression of the linear regime of the graphs give the spectral exponents  $\alpha$ . The results of the estimations are summarized in Table 1. In order to obtain a reasonably large linear scaling regime in the log–log plot for an accurate estimation of

the spectral exponent, the size of the images becomes a crucial factor. By considering square images of  $512 \times 512$  pixels, it is possible to examine the scaling law at least up to two decades in the wavenumber space.

Based on the FBS model, the spectral exponent  $\alpha$  can be expressed in terms of Hurst exponent using the relation  $\alpha = (2H + d_s)$  where  $d_s$  denotes the space filling factor (or more precisely the topological dimension of the space in which the object is embedded). A flat surface has  $d_s=2$  and a three-dimensional (3D) volume structure has  $d_s=3$ . The gray-level representation of an image can be treated as a three-dimensional pseudo-object mapped onto 2D surface with gray-levels as the compressed elevation variable.

The surface features of the first two samples, namely 20 and 22 wt% resemble the typical random surfaces. The spectral exponents therefore provide a consistent description of the textural variation observed in the first two compositions. As the water content is increased, the surface textures become more orderly with the formation of elongated texture morphologies which are no longer surfacelike. Despite the fact that there is no clear trend in the variation of the spectral exponent or the Hurst exponents, it is still possible to correlate the scaling exponents to the microstructures observed in the textures. The reduction in the Hurst exponents for example may be linked to formation of small-scale structures that appear as the sharp gray-level gradient in sample 24 wt% and onward. Nevertheless, we remarked that the isotropic model based on FBS with single global spectral exponent is not suitable for anisotropic images that contain large (elongated) and small (narrow) scale structures. The appearance of ordered structure in the form of networks or oily streaks makes the spectral exponents to vary in a complicated manner as water content is increased after 24 wt%.

## 4. Multifractal analysis

### 4.1. Generalized box-counting dimension

The main characteristic of fractal objects is their self-similar scaling property—the invariance under magnification for a wide range of temporal or length scales. For uniform fractal, the scaling is uniquely described by a single scaling exponent or fractal dimension  $D_B$  defined as

$$D_B = \lim_{\varepsilon \rightarrow 0} \frac{\ln N(\varepsilon)}{\ln(1/\varepsilon)}, \quad (13)$$

where  $\varepsilon$  is the lattice constant acting as non-overlapping covers of the structure under investigation, and  $N(\varepsilon)$  is the number of the cubes contained in the minimal cover.

The gray-level images are converted to black and white images by gray-level thresholding technique. The black pixels correspond to brighter areas of texture with gray-level pixel values from 77 and above (based on 30% thresholding). These bright areas are to be considered as information contents of the gray-level textures. In the black and white images, this information correspond to the black pixels. The criteria for choosing the threshold level is rather qualitative but it is motivated by the fact that it should not modify the information contents of the original image. Low threshold level

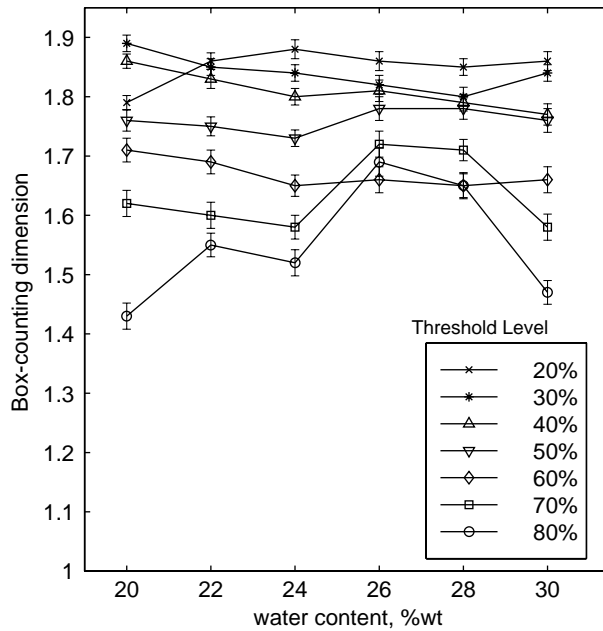


Fig. 6. The variation of fractal dimensions with different threshold levels used for converting gray-level images into black and white images.

preserves the small-scale features but gives redundant large-scales patterns. Meanwhile, high threshold levels cause the loss of small-scale features at the cost of preserving the large-scale information. We performed the thresholding at various levels and estimated the box-counting dimensions of the black and white images as shown in Fig. 6. This information is used to select an optimum threshold level for converting the gray-level images into black and white images for multifractal analysis based on generalized box-counting technique. We found that the 30% gray-level thresholding produced the set of images that exhibit consistent variation of box-counting dimension with respect to the space fillingness of the black pixels as we increased the water contents. Therefore this set of images will be used for the generalized box-counting analysis.

Most complex objects found in nature exhibit complicated scaling behaviors, which may be more suitably described by a spectrum of fractal exponents or the so-called generalized fractal dimensions  $D(q)$  as a function of a real number  $q$ . The fractal dimension is equal to  $D(0)$ , while  $D(1)$  and  $D(2)$  are the information and correlation dimensions, respectively. The function  $D(q)$  is generally referred to as a multifractal spectrum [21]. For 2D objects, the measure under study is encoded as a finite ensemble of points of the elemental dots or as black pixel for the case of black and white images [22,23]. An approximation of the probability measure then can be calculated as

$$p_k(\varepsilon) = \frac{N_k(\varepsilon)}{N}, \quad (14)$$

where  $N_k(\varepsilon)$  is the number of points falling into the  $k$ th box and  $N$  is the total number of dots or black pixels in the image. Multiscaling features are deduced by investigating the scaling behavior of this density distribution for different lattice sizes,  $\varepsilon \equiv l_j = 2^{-j}$ , with  $l_j$  is the length at scale  $2 < j < J$ . A digitized black and white image of the liquid crystal textures of size  $2^J \times 2^J$  is covered by  $N_{K,j}$  boxes of size  $l_j$ ,  $K = 2^{2(J-j)}$  and the content of each box is associated with measure  $p_k(l_j)$ . The generating function  $\chi(q, l)$  defines the multifractal scaling in terms of the exponents  $\tau(q)$ , which is given by

$$\chi(q, l) = l_j^{\tau(q)} \quad (15)$$

and can be calculated from the black pixel distribution information by using

$$\chi(q, l) = \sum_{k=1}^{N_{K,j}} [p_k(l_j)]^q. \quad (16)$$

The generalized fractal dimension is defined as

$$D(q) = \frac{\tau(q)}{q-1}. \quad (17)$$

First, the empirical generating function is estimated from the image using (16) and then the exponent  $\tau(q)$  is obtained using linear regression of the  $\log \chi(q, l)$  versus  $\log l_j$  for a set of different positive  $q$ -values. The plot of  $D(q)$  versus  $q$  is used to deduce the multifractal properties of the pixels distributions. A monofractal distribution would give  $D(q)$  as a constant, while multifractal distribution results in  $D(q)$  decreasing monotonically with increasing  $q$ . The procedure for calculating the multifractal spectrum for the textures of different compositions is carried out with  $q$  in a range from  $q_{\min} = 0.1$  to  $q_{\max} = 10.0$  in increments of 0.1, and the results are shown in Fig. 7. We noticed that  $D(q)$  is monotonically decreasing when the generating function satisfies the power-law (15) for a limited length scales within the range  $2^4 \leq l \leq 2^7$  for almost all the images and thus gives the desired characteristic of multifractality. Nevertheless, increasing the box size affects the accuracy of the estimation as indicated by the errorbars in Fig. 7 and this can be attributed to finite-size effect.

It is also interesting to note that the first three generalized dimensions namely  $D(0)$ ,  $D(1)$  and  $D(2)$  provide reasonably consistent descriptions of the morphological changes observed in the samples as observed in Fig. 8. Therefore, it can be concluded that the multifractal analysis on the black and white images provides useful interpretation of the multiscaling properties of complex textures such as those shown by the birefringence patterns of liquid crystals.

#### 4.2. Multifractal analysis of textures

Fractional Brownian surfaces have found numerous applications in computer modelling of rough surfaces in physics, material science, geology and medical imaging. One of the reasons for its success in modelling surfaces is due to the availability of fast and efficient algorithms that generates  $H$ -self-similar isotropic surfaces with stationary increments property [24]. Nevertheless, there are many situations where inhomogeneous

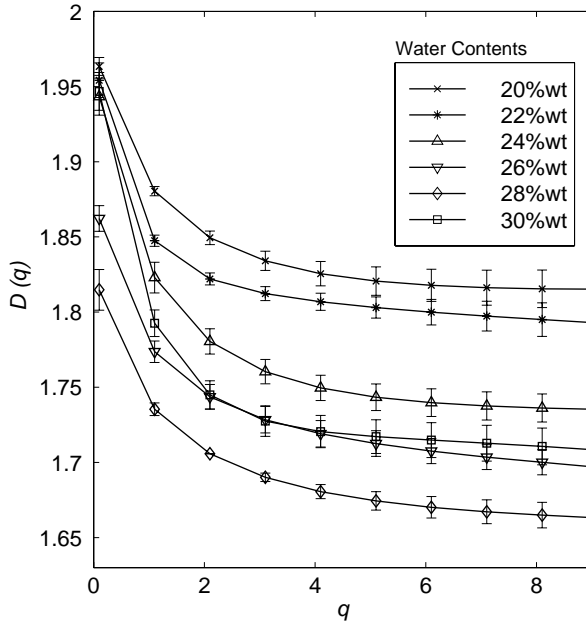


Fig. 7. Generalized box-counting dimensions for the textures of different compositions.

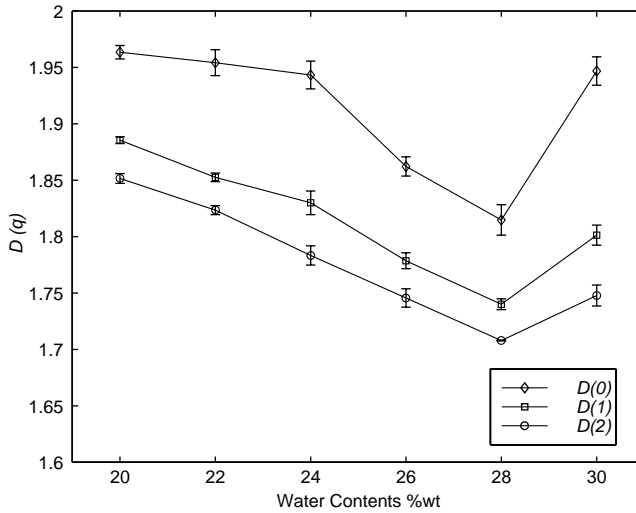


Fig. 8. Variations of  $D(0)$ ,  $D(1)$  and  $D(2)$  for different compositions.

textures are observed such as in medical images [25], satellite imagery [26] and geomorphology [27]. Under such circumstances, isotropic random surface generator such as the FBS may not be satisfactory.

One of the simplest fractal models that caters for this condition is the MBM, where the single value of  $H$  in (4) is replaced by a function  $H(\mathbf{x})$ ,  $\mathbf{x} \in R^2$  [28,29]. MBM in 1D is defined as

$$B_{H(x)}(x) = \frac{1}{\Gamma(H(x) + 1/2)} \left\{ \int_{-\infty}^0 [(x - x')^{H(x)-1/2} - (-x')^{H(x)-1/2}] dB(x') + \int_0^x (x - x')^{H(x)-1/2} dB(x') \right\} \quad (18)$$

with space (or time) -varying Hurst function  $H : [0, \infty) \rightarrow (0, 1)$ . The covariance of a normalized MBM takes the following form

$$\langle B_{H(x)}(x) B_{H(y)}(y) \rangle \sim \frac{1}{2} [|x|^{H(x)+H(y)} + |y|^{H(x)+H(y)} - |x - y|^{H(x)+H(y)}] \quad (19)$$

and MBM does no longer has stationary increments. Nevertheless, it can be shown that MBM is asymptotically locally self-similar with local fractal dimension on any interval  $[a, b]$  equal to  $2 - \min\{H(x), x \in [a, b]\}$ . This process can be extended to a 2D isotropic inhomogeneous Gaussian random surface generator with covariances in the form of [30,31]

$$\langle B_{H(\mathbf{x})}(\mathbf{x}) B_{H(\mathbf{y})}(\mathbf{y}) \rangle \sim \frac{1}{2} [\|\mathbf{x}\|^{H(\mathbf{x})+H(\mathbf{y})} + \|\mathbf{y}\|^{H(\mathbf{x})+H(\mathbf{y})} - \|\mathbf{x} - \mathbf{y}\|^{H(\mathbf{x})+H(\mathbf{y})}] \quad (20)$$

with  $H(\mathbf{x})$ ,  $\mathbf{x} \in R^2$ . Anisotropic as well as inhomogeneous surface can be obtained by considering the tensor of two 1D-FBM with Hurst exponents  $H(x)$  and  $H(x)$  in  $x$ - and  $y$ -direction, respectively [30] but this model will not be considered here.

Based on the 2D-MBM model, the local Hurst exponents  $H(x_1, x_2)$  are estimated using the multifractal image segmentation routine in FRACLAB [32]. Since the local regularity of an image of  $N \times N$  pixels is now given by the  $N \times N$  Hurst exponents matrix, a direct comparison of the latter for different textures becomes difficult. For this reason, we compared the ensemble averaged normalized histogram of Hurst exponents as shown in Fig. 9. The standard deviation of the estimation errors is less than 10% for all four compositions considered here. It is observed that the rougher textures are attributed to dominance of smaller values of Hurst exponents in the image histogram at lower water content. Further increasing of water concentration turned the surface-like structures into network-like morphologies, making the 2D-MBM model to break down at 26 wt%.

## 5. Discussions and conclusions

The surface textures of birefringence patterns of liquid crystal reveal a great deal of information about molecular ordering in different phases. Image analysis based on fractal and multifractal techniques are becoming an integral part of many material surface characterization software. Fractal dimension and the related scaling exponents such as Hurst exponent have been shown to be useful measurable image parameters that can be linked to physical properties.

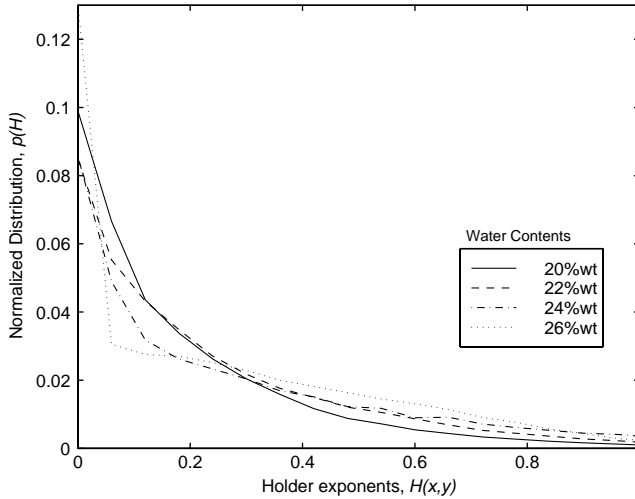


Fig. 9. Normalised histogram of the occurrence of local Hurst exponents  $H(x, y)$  in the images.

In this work, we have investigated the applications of fractal geometry to characterize birefringence patterns. Distinctive features in the textures were observed in the lyotropic lamellar liquid crystal system (water/cethylpyridinium chloride/decanol) that showed a gradual transition from mosaic to oily streak structures and then to maltese cross texture upon increasing the water contents. These textures were first characterized using Fourier spectrum method and the power-law scaling behavior is referred to a particular monofractal model namely the fractional Brownian sheet. The spectral exponent  $\alpha$  is linked to the fractal dimension  $D$  and the Hurst exponent  $H$  through the relations  $\alpha = 2H + 2$  and  $D = 3 - H$ ,  $0 < H < 1$ . In order for these image parameters to be consistent with the morphological features observed such as the surface- and line-like structures, a simple interpretation of the results was given. Upon acknowledging the fact that most complex surfaces are inhomogeneous and/or anisotropic, a multifractal analysis using generalized box-counting technique was given. The first three generalized dimensions namely the fractal dimension  $D(0)$ , information dimension  $D(1)$  and correlation dimensions  $D(2)$  suggest that the birefringence textures exhibit multifractal properties and this can be inferred from the monotonically decreasing of  $D(q)$  with respect to increasing  $q$ . An alternative view to multifractal scaling has been suggested with the introduction of MBM the modelling of inhomogeneous processes or surfaces. Despite the advantage of providing a more natural description of complex surfaces, the application of MBM in the characterization of material surfaces is still not well known.

The scope of applications of fractal analysis in material science is not restricted to surfaces or curves. In order to be able to link the scaling exponents obtained from fractal analysis to material properties, it is crucial to understand the microscopic and/or the bulk features of the materials. The formation of mesophases can be viewed as a complicated random process that produces structures that are self-similar in the sense

that the two-point density–density correlation function [33]

$$C(r) = \frac{1}{N} \int_V \langle \rho(r') \rho(r' + r) \rangle d^3 r' \\ \sim r^{D-3}, \quad (21)$$

where  $D$  is the fractal dimension,  $\rho$  is the particle density inside the fractal aggregate,  $r$  is the inter-particle distance,  $V$  is irradiate volume of the sample and  $N$  is the total number of particles in the fractal aggregate given by

$$N = \int_V C(r) V(r) d^3 r. \quad (22)$$

Light scattering experiments show that the intensity of scattering  $I(Q)$  from a single fractal is given the Fourier transform of the density–density correlation function:

$$I(Q) \propto N \int_V V C(r) \exp(i\mathbf{Q} \cdot \mathbf{r}) d^3 r \\ \sim Q^{-D}, \quad (23)$$

where  $|\mathbf{Q}| = Q = 4\pi n \lambda^{-1} \sin(\theta/2)$ ,  $n$  is the refractive index,  $\lambda$  is the wavelength of the incident beam, and  $\theta$  is the scattering angle.

We note that the samples with 30 wt% water content exhibit homeotropic alignment with the presence of typical oily streaks defects and maltese crosses, which are characteristic features of lamellar phases. At a low viscosity, lamellar lyotropic liquid crystal  $L_\alpha$  phase is indicated by the presence of focal conics defects and the oily streaks formed by nucleation of focal conics. With the decrease of water contents from 30 to 26 wt%, the liquid crystal changes gradually from flowing to non-flowing, stiff gel-like lamellar phase. Under polarizing microscope, the changes are marked by formation of rigid defect networks. To our knowledge, there exist two models that have been proposed to account for the oily streaks structures. In the disclination model, oily streaks are modelled as pairs of disclinations corresponding to a dislocation [34,10], whereas in the Friedel model [35] oil streaks are described as aggregates of focal conic domains. By further decreasing the water contents to 24 and 22 wt%, the lamellar phase turned into highly viscous gel-like liquid crystal. The formation of bright areas in the birefringence field suggests the presence of dense ultrafine line defects embedded in the stiff gel-like lamellar phase. Similar textural transition has been reported by Warriner et al. [36] in polymer-lipid lyotropic lamellar liquid crystalline system.

To summarize, we have presented a few alternatives in the fractal and multifractal analysis of image textures. It would be interesting to further explore the advantage of using such techniques in the understanding of microscopic properties of the material under consideration. Studies have shown that fractal analysis is useful for differentiating various types of growth dynamics in colloidal and liquid crystal systems [37,33] or characterizing defect structures when combined with other multiscaling techniques such as wavelet analysis [38,39]. Further investigation along this direction may elucidate the applications of self-similar processes for dynamical modelling of disordered phenomena.

## Acknowledgements

We thank the Malaysian Ministry of Science, Technology and Environment for the research grants IRPA 09-02-02-0092 and IRPA 09-02-02-0091, Ismail Bahari of UKM for the microscopy facility and the Microscopy Unit of National University of Singapore for assistance with the freeze fracture study.

## References

- [1] A. Saucier, J. Muller, *Physica A* 267 (1999) 221.
- [2] B.B. Mandelbrot, *The Fractal Geometry of Nature*, Freeman, New York, 1982.
- [3] S. Davies, P. Hall, J. Roy. Statist. Soc. B 61 (1) (1999) 3.
- [4] A.P. Pentland, *IEEE Trans. Pattern Anal. Mach. Intell.* 6 (1984) 661.
- [5] D. Osman, D. Newitt, A. Gies, T. Budinger, V.H. Truong, S. Majumdar, J. Kinney, *Fractals* 6 (1998) 275.
- [6] A.L. Barabasi, H.E. Stanley, *Fractal Concepts in Surface Growth*, Cambridge University Press, Cambridge, 1995.
- [7] W. Zahn, A. Zosch, *Fresenius J. Anal. Chem.* 365 (1997) 119.
- [8] S. Chandrasekhar, *Liquid Crystals*, Cambridge University Press, Cambridge, 1992.
- [9] P.G. de Gennes, *The Physics of Liquid Crystal*, Clarendon Press, Oxford, 1993.
- [10] P. Boltenhagen, O.D. Lavrentovich, M. Kleman, *J. Phy. II Fr.* 1 (1991) 1233.
- [11] M. Tuceryan, A.K. Jain, *Handbook of Pattern Recognition and Computer Vision*, World Scientific, Singapore, 1993.
- [12] D. Demus, L. Richter, *Texture of Liquid Crystals*, Verlag Chemie, New York, 1978.
- [13] B.B. Mandelbrot, *J. van Ness*, *SIAM Rev.* 10 (1968) 422.
- [14] L.M. Kaplan, C.C.J. Kuo, *IEEE Trans. Image Process.* 5 (1996) 754.
- [15] H. Qian, G.M. Raymond, J.B. Bassingthwaight, *J. Phys. A* 31 (1998) L527.
- [16] P. Flandrin, *Time-Frequency/Time-Scale Analysis*, Academic Press, San Diego, 1998.
- [17] P. Flandrin, *IEEE Trans. Inform. Theory* 35 (1989) 197.
- [18] D.E. Passoja, D. Psioda, in: L.N. Gilbertson, R.D. Zipp (Eds.), *Fractography and Materials Science*, American Society for Testing and Materials, Philadelphia, 1981.
- [19] G. Chan, P. Hall, D.S. Poskitt, *Ann. Statist.* 23 (1995) 1995.
- [20] W.H. Press, S.A. Teukolsky, W.T. Vetterling, B.P. Flannery, *Numerical Recipes in Fortran: The Art of Scientific Computing*, Cambridge University Press, Cambridge, 1992.
- [21] H.G.R. Hentschel, I. Procaccia, *Physica D* 8 (1983) 435.
- [22] J. Muller, *J. Hydrol.* 187 (1996) 215.
- [23] Z.W. Chen, X.P. Wang, S. Tan, S.Y. Zhang, J.G. Hou, Z.Q. Wu, *Phys. Rev. E* 63 (2001) 165413.
- [24] D.R. McGaughey, G.J.M. Aitken, *Physica A* 311 (2002) 369.
- [25] R. Jennane, W.J. Ohley, S. Majumdar, G. Lemineur, *IEEE Trans. Med. Imaging* 20 (2001) 443.
- [26] J. Ilow, H. Leung, *IEEE Trans. Image Process.* 10 (2001) 792.
- [27] N.S.N. Lam, D.C. Lee, *Fractals in Geography*, Prentice-Hall, Englewood Cliffs, NJ, 1993.
- [28] R. Peltier, J. Levy-Vehel, *INRIA Research Report*, 2645, 1995.
- [29] A. Benassi, S. Jaffard, D. Roux, *Rev. Mat. Iberoamericana* 13 (1997) 19.
- [30] B. Pesquet-Popescu, J. Levy-Vehel, *ENST preprint*, 2002.
- [31] E. Herbin, *INRIA preprint*, 2002.
- [32] <http://www-rocq.inria.fr/fractales/Software/FRACLAB/fraclab.html>.
- [33] D. Tezak, M. Martinis, S. Puncce, I. Fischer-Palkovic, F. Strajnar, *Liq. Cryst.* 19 (2) (1995) 159.
- [34] M. Kleman, C.E. Williams, *Philos. Mag.* 35 (1) (1977) 33.
- [35] G. Friedel, *Ann. Phys. Paris* 2 (1992) 273.
- [36] H.E. Warriner, S.H.J. Idziak, N.L. Slack, P. Davidson, C.R. Safinya, *Science* 271 (1996) 969.
- [37] M. Vicsek, T. Vicsek, *Fractal Growth*, World Scientific, Singapore, 1992.
- [38] A.C. Newell, T. Passot, J. Lega, *Annu. Rev. Fluid Mech.* 25 (1993) 399.
- [39] C. Bowman, N. Ercolani, R. Indik, Alan C. Newell, T. Passot, *Physica D* 123 (1998) 474.